J Electroceram (2010) 25:159–167
DOI 10.1007/s10832-010-9607-6

Electrospun SnO_2 nanofiber mats with thermo-compression step for gas sensing applications

Il-Doo Kim · Eun-Kyung Jeon · Seung-Hoon Choi · Duck-Kyun Choi · Harry L. Tuller

Received: 14 June 2008 / Accepted: 14 April 2010 / Published online: 24 April 2010

Abstract SnO_2 nanofiber mats fabricated through electrospinning followed by thermo-compression and subsequent calcination steps exhibited unique morphologies facilitating efficient gas transport into the layers combined with high surface area (~73.5 m^2/g, measured by BET) and small grain size (~5–15 nm), which are well suited for ultrasensitive gas detection. Single SnO_2 nanofibers were found to have a belt-like structure of closely packed nanocrystallites, facilitating excellent adhesion to the substrate and good electrical contact to the electrodes. I–V measurements of single SnO_2 nanofibers displayed ohmic behavior with electrical conductivity of 1.5 S/cm. Gas sensor prototypes comprising a random network of SnO_2 fibers exhibited high sensitivity when exposed to NO_2 at 225°C and CO at 300°C. A detection limit of 150 ppb NO_2 at 185°C was estimated by extrapolating the sensitivity results obtained on exposure to higher gas concentrations, demonstrating potential of achieving ultra-sensitive gas detection at low operating temperatures enabled by the present synthesis method.

Keywords Electrospinning · Sensor · SnO_2 · Nanofiber mats

I.-D. Kim (✉) · S.-H. Choi
Optoelectronic Materials Center,
Korea Institute of Science and Technology,
PO Box 131, Cheongryang,
Seoul, Republic of Korea
e-mail: idkim@kist.re.kr

E.-K. Jeon · D.-K. Choi
Department of Materials Science and Engineering,
Hanyang University,
Hangdang-dong,
Seoul, Republic of Korea

H. L. Tuller
Department of Materials Science and Engineering,
Massachusetts Institute of Technology,
77 Massachusetts Ave.,
Cambridge, MA 02139, USA
e-mail: tuller@mit.edu

1 Introduction

Significant progress has recently been achieved in developing highly sensitive chemical sensors using novel nanostructured architectures [1–5]. In particular, a lot of research efforts have focused on the development of one-dimensional (1D) and quasi-1D building blocks and their controlled assembly into nanostructured devices by combining top-down and bottom-up nanofabrication processes. However, the incorporation of 1D nanosized elements such as single crystalline nanowires [6, 7], nanobelts [8, 9], nanotubes [10, 11], and nanofibers [12–14], into electronic devices presents great challenges in achieving good and reliable electrical contacts. Among the different strategies for producing devices based on nanosized 1D building blocks electrospinning offers several advantages including ease of fabrication and robustness due to fiber network redundancy. Nanofibrous ceramic layers produced by electrospinning of polymer/ceramic composite fibers display unique quai-1D nanocrystalline morphologies that give rise to high surface area and large surface-to-volume ratio, offering effective gas modulation of device resistance [12, 15, 16].

Electrospinning is one of the most versatile methods for producing polycrystalline nanofibers from a rich variety of materials including TiO_2 [12], SnO_2 [13], WO_3 [14], SnO_2-TiO_2 bi-component nanowires [17], MoO_3 [18], ZnO [19], and metal modified TiO_2 nanofibers [20]. By adding inorganic precursors to the electrospun polymer solution, polymer fibers can be transformed into inorganic

fibers, following calcination in air at elevated temperatures (≥450°C). While there have been some early promising results for applying electrospun MoO_3 and WO_3 nanofibers to gas sensors [21, 22], they still do not meet the requirements of ultrasensitive sensors capable of detecting trace concentrations of gases in the parts per billion (ppb) range and below. In particular, poor adhesion between the electrospun fibers and substrates is a major barrier for the realization of stable sensing architectures. To satisfy the dual requirements of improved electrical contact and markedly reduced nanofiber cross-section [23, 24], the authors recently introduced an electrospinning process modification [12], offering dimensional control over nanofibril diameter as well as structural morphology (controlled grain size and pore size distributions) [15]. This unique morphology facilitates effective penetration of the surrounding gas into the porous ceramic layer, which is believed to be the main reason for the exceptionally high gas sensitivity of TiO_2 gas sensors produced by this method [12, 15]. Unlike conventional screen printing methods that produce mesoporous granular layers with densely packed nanoparticles that give rise to poor gas transport [25], sensors produced by electrospinning display a bi-modal pore size distribution comprising both large and small pores that enhance gas transport and sensitivity in these layers [12, 15].

A major drawback of the previously investigated electrospun TiO_2 sensors, however, was their high base resistance in the range of giga-ohms (10^9 Ω) at 300°C, creating challenges for signal acquisition [12, 15]. By reducing device resistance by several orders of magnitude, while maintaining the unique nanofibrous morphology, one can envision operation at temperatures as low as 200°C, well below the typical application range for many microscaled gas sensor devices. In this regard, the fabrication of tin dioxde (SnO_2) nanofiber mats by electrospinning followed by thermo-compression and calcination steps, and their response to NO_2 and CO in the temperature range from 125°C to 450°C, are presented in this work. Furthermore, we report on the clear evidence of the formation of a belt-like structure in single SnO_2 nanofibers following the thermo-compression step. This leads to improved adhesion of electrospun nanofibers to planar substrates and better electrical contact to the electrodes.

2 Experimental

Electrospun SnO_2 chemiresistor mats were prepared by the procedure previously reported by the authors involving the electrospinning of polymer solution followed by a thermo-compression step at 120°C [12]. In the first step, $Sn(Ac)_4$/PVAc, i.e. tin acetate and poly(vinyl acetate) (PVAc, Mw= 1,300,000 g/mol), composite fiber mats are electrospun from a mixed solution of dimethyl formamide (DMF) and acetic acid. In this process, the precursor solution is transferred into a syringe mounted on the electrospinning apparatus. A high voltage of 10~12 kV is applied between the syringe tip and the substrate, resulting in the emission of a continuous fiber stream. The syringe is rastered, in an x-y fashion, over the substrate resulting in a three dimensionally interconnected fiber mats.

Thermogravimetric studies were carried out using a TG-2050 thermal analyzer system (Ta instruments, Inc.) at a heating rate of 10°C/min. As shown in Fig. 1, thermogravimetric analysis (TGA) curve (temperature range: 0~800°C) exhibited three distinct stages of weight loss. The first weight loss began at 199.4°C due to evaporation of water and residual solvent, i.e. DMF. The second weight loss step, observed around 280°C, was attributed to the degradation of PVAc by a deacetylation of VAc(vinylacetate) groups, i.e., elimination of acetic acid, to form polyacetylene segments in the backbone. The weight loss around 290°C corresponded to further degradation of unsaturated backbone residues and the burning out of organic composites. The total weight-loss evaluated by TGA was about 72.24%. The crystal structure of the SnO_2 nanofiber mats (prepared on stainless steel substrates) was investigated by X-ray diffractometry (XRD, Rigaku D/MAX-RC; with CuKα radiation). The microstructure development during the process steps was followed by scanning electron microscopy (JSM-6330F, JEOL). A focused ion beam (FIB, Nova 600, FEI Inc.) was used to expose the cross section of a single SnO_2 nanofiber and SnO_2 nanobelt, respectively.

Transmission electron microscopy (TEM) was used to examine the microstructure of the SnO_2 nanofibers, while

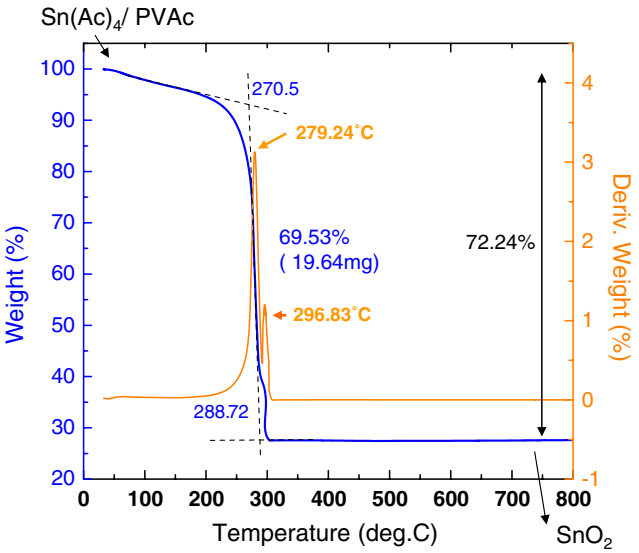

Fig. 1 Thermogravimetric analysis (TGA) curve (temperature range: 0~800°C) exhibited three distinct stages of weight loss

individual grain structures were examined by high resolution TEM (Tecnai G2, FEI Hong Kong Co., Ltd.). Ultra-sonication was used to disperse the SnO_2 nanofibers in ethanol followed by mounting on a carbon-coated Cu grid. Brunauer-Emmett-Teller (BET, Sorptomatic 1990, ThermoFinnigan) analysis was carried out to investigate the specific surface area. Current-voltage (I–V) characteristics were examined with an Agilent B1500 semiconductor parameter analyzer. The gas sensing experimental setup is described elsewhere [12].

3 Results and discussion

SnO_2 fibers were electrospun onto SiO_2/Si substrates and thermo-compressed at 120°C and calcined at 450°C in order to investigate the structural changes during the thermo-compression step. As shown in Fig. 2(a), a Field Emission SEM (FE-SEM) micrograph shows the SnO_2 nanofiber prepared without thermo-compression to have a diameter of 270 nm and grain size on the order of 5–15 nm. Focused Ion Beam (FIB) micro-milling was used to examine the cross sectional view of a single SnO_2 nanofiber. As shown in the inset of Fig. 2(a), an ellipsoidal cross section with a major axis of 270 nm and minor axis of 150 nm was obtained, likely due to the partial melting of the $Sn(Ac)_4$/PVAc composite fiber during the calcination step. On the other hand, SnO_2 nanofibers fabricated with a thermo-compression step prior to the calcination step exhibited a belt-like structure as shown in Fig. 2(b). A cross sectional view of a single SnO_2 fiber is shown in the inset of Fig. 2(b). The height (80 nm) of the fiber is much smaller than its width (2.1 μm), demonstrating a nano-crystalline belt-like structure that most likely results from a complete melting of the $Sn(Ac)_4$/PVAc composite nanofiber during the thermo-compression step at 120°C.

In order to investigate the electrical conductivity of a single SnO_2 nanobelt, Al electrodes were patterned on top of individual SnO_2 nanobelts with the aid of a shadow mask. The line width of each Al electrode was 2,000 μm, spaced 65 μm apart, as shown in the confocal micrograph in Fig. 2(c). The electrical conductivity of a single SnO_2 nanobelt can be estimated from the expression, $\sigma = \frac{1}{R} \times \frac{l}{A}$, where R is the resistance, A the cross sectional area ($A=ab$ with a the width and b the height of the SnO_2 nanobelt), and l the distance between the electrodes. A nearly linear relationship between current and voltage was obtained (at ambient temperature), as shown in Fig. 2(d), with an electrical conductivity of 1.5 S/cm. Compared to the electrospun TiO_2 sensors studied reported in Refs. [12] and [15] the SnO_2 fiber mats display a much lower overall

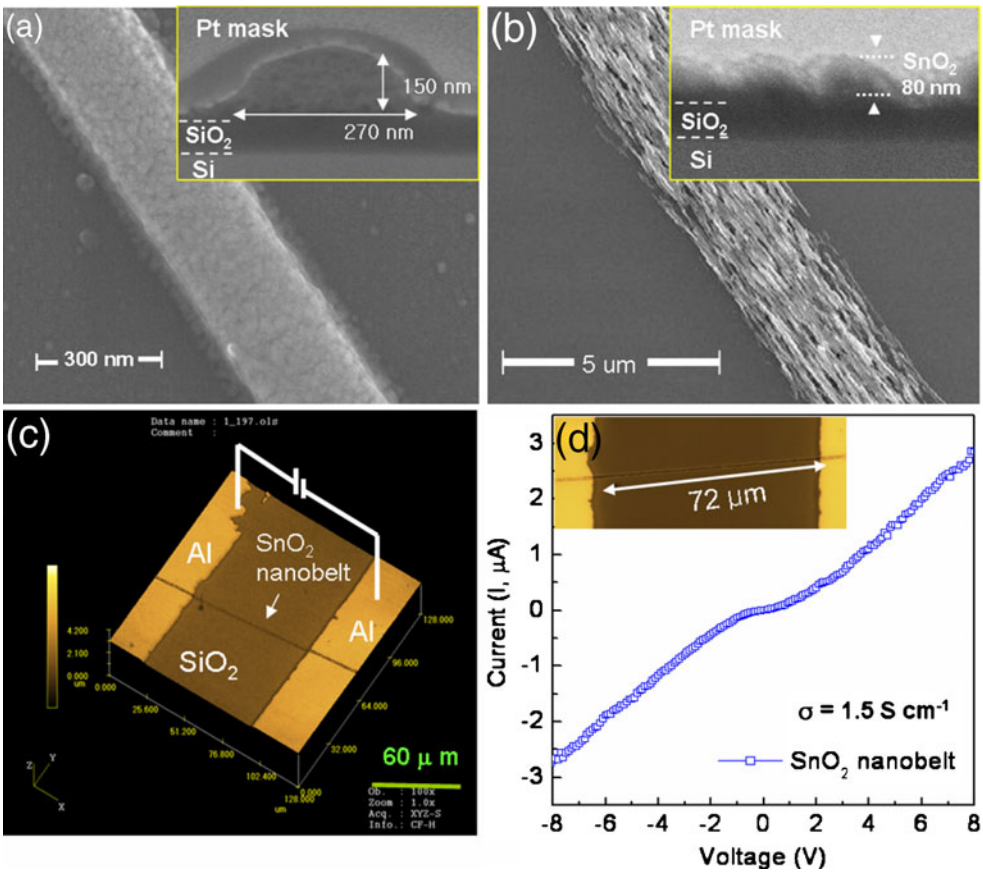

Fig. 2 (**a**) SEM image of calcined SnO_2 nanofiber prepared on SiO_2/Si substrates without thermo-compression. The inset emphasizes cross sectional view of an individual SnO_2 nanofiber micromilled by focused ion beam. (**b**) SEM image of calcined SnO_2 nanofiber prepared through a thermo-compression step. The inset emphasizes a cross sectional view of an individual SnO_2 nanobelt-like structure micromilled by focused ion beam. (**c**) Surface morphology with patterned Al electrodes scanned by confocal microscope. The interval between Al electrodes is 65 μm. (**d**) I–V characteristics between pairs of electrodes

resistance by at least 4 orders of magnitude. This simplifies the electrical measurements and reduces the noise, enabling a lower detection limit.

To fabricate gas sensor prototypes, the precursor solution was directly electrospun onto Au (150 nm)/Ti (50 nm)/SiN (150 nm)/SiO_2 (300 nm)/Si substrates. The Au-interdigitated electrodes (IDE) had 20 fingers separated by 10 or 20 μm spacings. The as-spun $Sn(Ac)_4$/PVAc composite fiber mats were then thermo-compressed using preheated plates at 120°C for 10 min, followed by calcination at 450°C for 30 min in air. The processing procedure is illustrated in Fig. 3.

Figure 4 shows SEM images of SnO_2 fiber mats deposited on Au (150 nm)/Ti (50 nm)/SiNx (150 nm)/SiO_2 (300 nm)/Si interdigitated electrodes arrays following heating at 450°C for 30 min. The as-spun $Sn(Ac)_4$/PVAc composite fibers (see Fig. 4(a)) exhibit a range of diameters between 200 and 400 nm. Without the thermo-compression step, but after calcination at 450°C in air for 30 min to decompose the PVAc, the SnO_2 fibers exhibited a regular fibrillar structure composed of 200–400 nm diameter cores as shown in Fig. 4(c). High resolution SEM images reveal the nanostructured morphology of the fibers, composed of densely packed nanoparticles with the diameters of ~15 nm (see Fig. 4(e)). The as-spun SnO_2 fiber mats exhibited poor adhesion to the substrates and following calcination at 450°C they tended to peel off from the substrates. In order to rectify this problem, a thermo-compression procedure was introduced prior to the calcination step. This served to drive the PVAc above its glass transition temperature (28–30°C), resulting in markedly improved adhesion to the substrate. As a consequence, the thermo-compressed fibers did not peel off during handling and testing. An interconnected morphology of the $Sn(Ac)_4$/PVAc composite fiber was obtained due to the melting of the PVAc as shown in Fig. 4(b). Subsequent calcination at 450°C for 30 min resulted in porous structures with high surface area as shown in Fig. 4(d). The SnO_2 nanofiber mats consist of nanograins in the range of 5–15 nm (average ~10 nm) and similarly nanosized pores. As shown in Fig. 4(f), highly porous fibers with loosely packed nanoparticle were obtained following the thermo-compression and annealing steps, compared to the granular fibers comprising densely packed nanoparticles obtained without the thermo-compression step (see Fig. 4(e)). The bi-modal pore size distribution comprising large and small pores (see Fig. 4(d) and (f), respectively) provides easy pathways for efficient gas transport into the inner part of the layer while at the same time maintaining high surface area and surface-to-volume ratio that favorably contribute to surface activity and gas sensitivity [26, 27]. Therefore, the gas sensitivity of the thermo-compressed fibers structure is expected to be superior to that obtained without thermo-compression.

The crystallization of the electrospun SnO_2 nanofiber mats was examined by XRD analysis in the range of 2θ

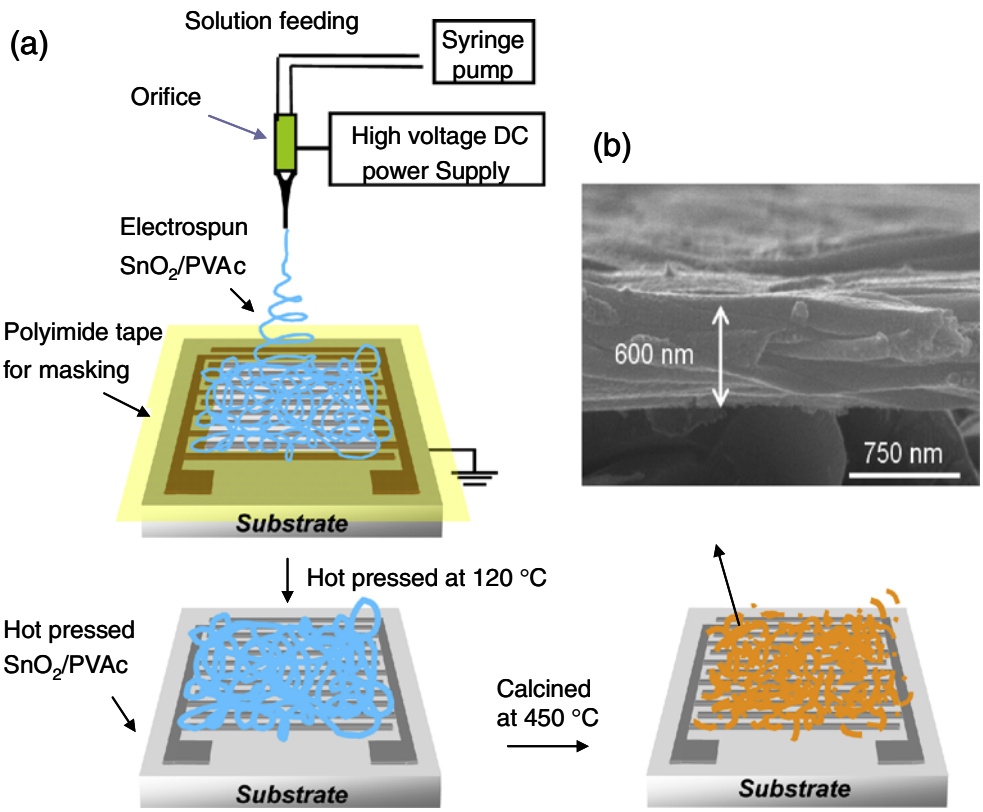

Fig. 3 (**a**) Schematic diagram of the processing steps used to fabricate SnO_2 nanofiber mats on Au coated Si substrates. The steps include electrospinning, thermo-compression, and calcination (**b**) Cross-sectional SEM micrograph of SnO_2 nanofiber mats thermo-compressed at 120°C and calcined at 450°C for 30 min

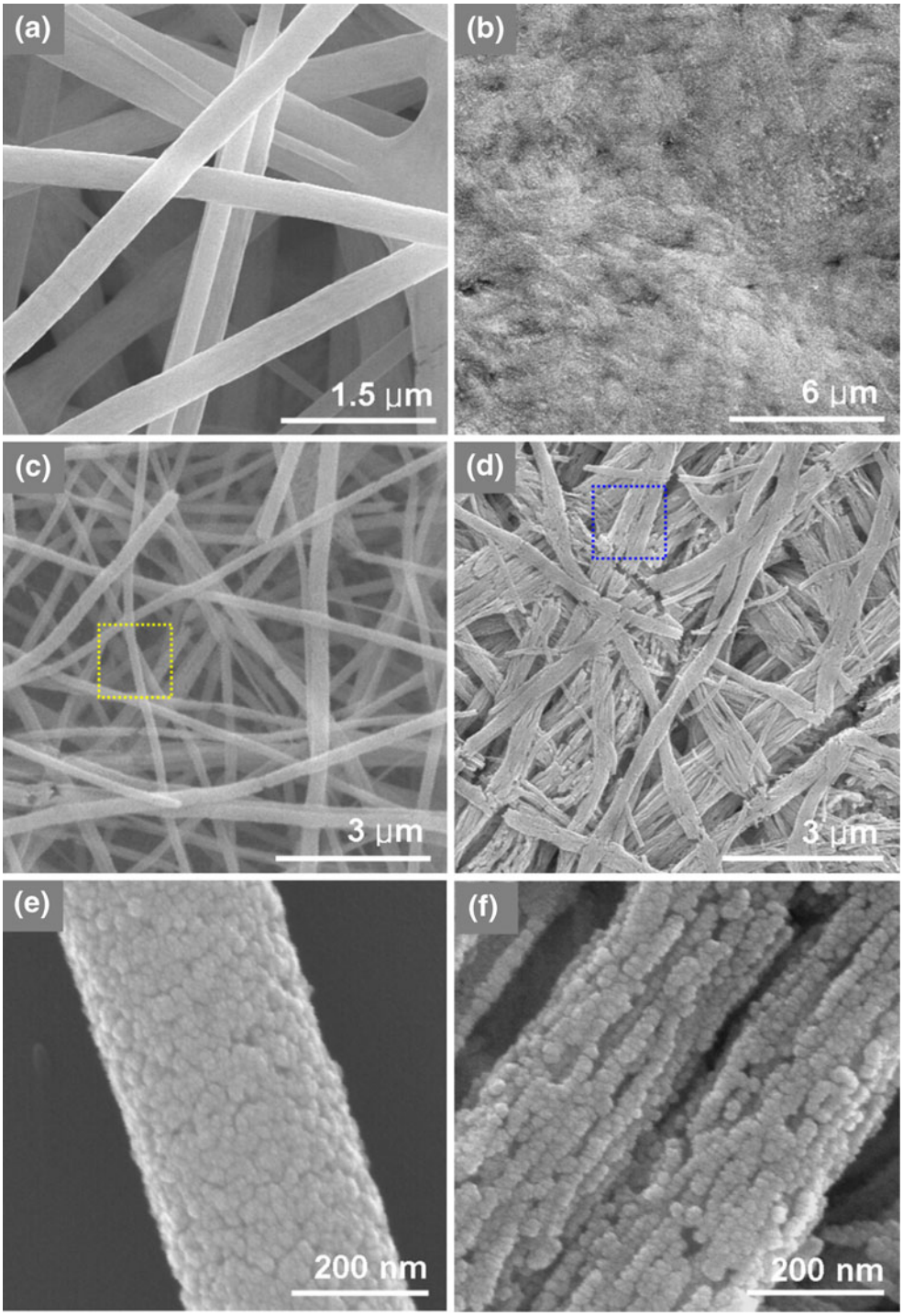

Fig. 4 (**a**) SEM image of the as-spun $Sn(Ac)_4$/PVAc composite nanofiber mats prepared by electrospinning. (**b**) SEM image of $Sn(Ac)_4$/PVAc composite nanofiber mats after thermo-compression at 120°C for 10 min. (**c**) SEM image of SnO_2 nanofiber mats calcined at 450°C without thermo-compression step. The inset shows the image of an individual SnO_2 nanofiber. (**d**) SEM image of SnO_2 nanofiber mats thermo-compressed at 120°C and calcined at 450°C. The inset shows the image of individual SnO_2 nanofibers. (**e**) High magnification SEM image of an individual SnO_2 nanofiber in dotted area of Fig. 4(c). (**f**) High magnification SEM image of an individual SnO_2 nanofiber in dotted area of Fig. 4(d)

between 20° and 60°. The XRD spectra in Fig. 5 show that the electrospun SnO_2 fiber mats crystallized into the rutile structure with primary (110), (101), and (211) crystallite orientations. According to the Scherrer equation ($D = 0.94\lambda_x/\beta\cos\theta$ where D is the mean grain size, 2θ is diffraction angle and λ_x is the X-ray wavelength, β is the full width at half maximum of the diffraction peak), the SnO_2 fibers had a mean grain size of about 8.4 nm.

The microstructure of hot-pressed and calcined SnO_2 fiber mats was examined by high-resolution transmission electron microscopy (HRTEM). Figure 6(a) shows a TEM micrograph of the tip of a SnO_2 nanofiber made up of 5–15 nm sized grains. Lattice images are clearly observed in Fig. 6(b), indicating that the SnO_2 fibers are highly crystalline. The inset of Fig. 6(c) shows the electron diffraction pattern obtained by Fast Fourier transform

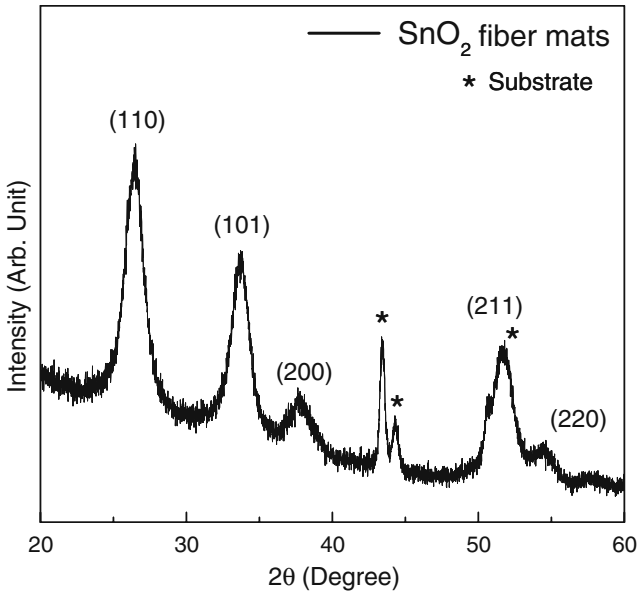

Fig. 5 X-ray diffraction pattern of SnO_2 nanofiber mats calcined at 450°C for 30 min. electrospun SnO_2 fiber mats crystallized into the rutile structure with primary (110), (101), and (211) peaks

(FFT) of the lattice image from a single grain. The electron diffraction spots are indexed based on the rutile structure. The lattice distance was measured as 3.35 Å and 2.64 Å corresponding to the (110) and (011) planes of SnO_2 rutile (see Fig. 6(d)). The measured angle between the (011) and (101) planes was 47°, consistent with the SnO_2 rutile structure.

In order to examine the gas sensitivity of the electrospun SnO_2 sensor prototypes against traces of NO_2 and CO, the specimens were mounted on Al_2O_3 sample holders and inserted inside a quartz tube placed inside a tube furnace. The samples were heated in air to temperatures between 125°C and 450°C. Gas mixtures of 100 ppm NO_2 or 1,000 ppm CO in air served as the analytes. These were then mixed with dry air (total flow: 200 sccm/min) to achieve the final desired analyte concentrations. Details of the measurement cycle are given in Ref. [12].

Figure 7(a) shows the resistance response of a SnO_2 sensor upon exposure to successive cycles (10 min exposure followed by 50 min recovery in dry air) of CO at 300°C. The CO concentration was increased from 5 to 500 ppm as indicated in the top part of the figure. The sign of the sensor

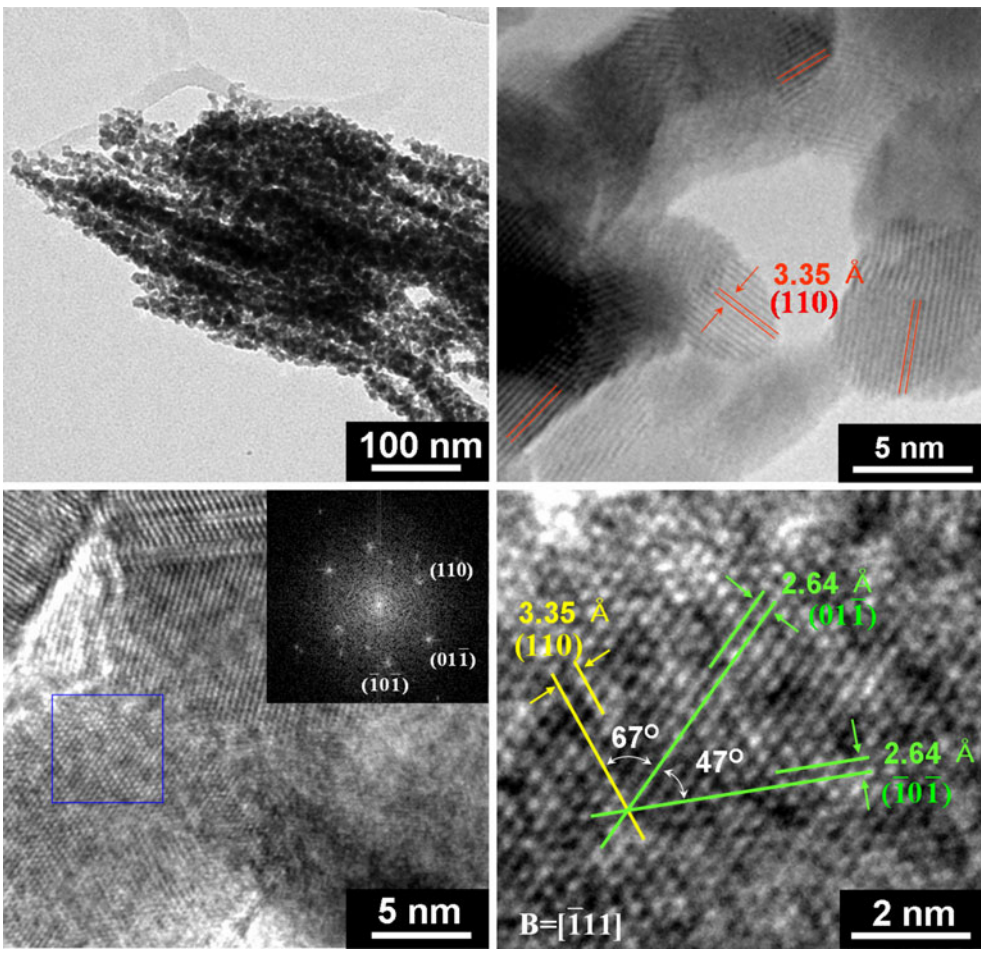

Fig. 6 (**a**) TEM microstructure of SnO_2 nanofiber mats obtained after thremo-compression step and calcination. (**b**) TEM micrographs of individual SnO_2 nanograins comprising SnO_2 nanofiber mats (**c**) Magnified HR-TEM image. The inset shows FFT electron diffraction pattern obtained from part c. (**d**) Lattice image of a single crystalline SnO_2 grain

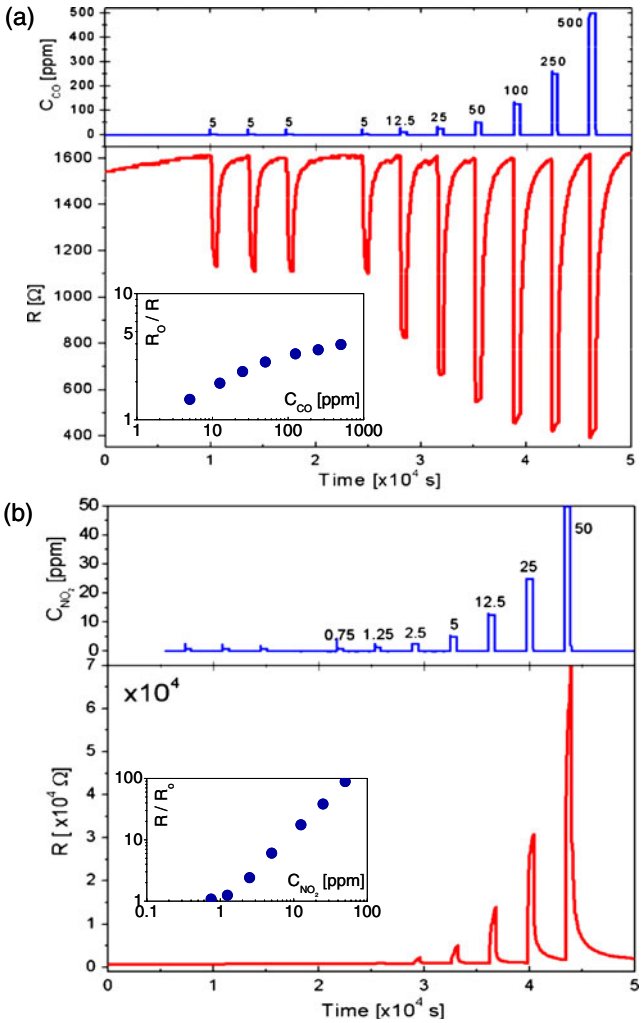

Fig. 7 (**a**) Resistance response upon exposure to CO at 300°C. Top: corresponding analyte concentration. Sample: SnO_2 nanofiber mats on Si wafer with Au-IDE. The inset emphasizes response towards CO at 300°C, double-logarithmic representation. (**b**) Resistance response upon exposure to NO_2 at 225°C. Top: corresponding analyte concentration. Sample: SnO_2 nanofiber mats on Si wafer with Au-IDE. The inset emphasizes sensor response to NO_2 at 225°C in double-logarithmic representation

response, i.e., lower resistance when exposed to CO than the baseline resistance in air, is in agreement with the expected behavior of *n*-type metal oxide gas sensors in the presence of reducing gases [28, 29]. The relatively low baseline resistance R_0 in dry air (1.6 kΩ at 300°C) is attributed, in part, to the small electrode spacings (10 and 20 μm) of the Au-IDE structures as well as to the relatively low resistivity of SnO_2 in dry air atmospheres. For each cycle, we calculate the sensitivity values, defined here as the relative sensor conductance G/G_0 (=R_0/R) or resistance R/R_0 upon exposure to reducing or oxidizing gases, respectively, where R_0 is the sensor resistance in air just before introducing the test gas to the system and R is the minimum (maximum) resistance during exposure to a given reducing (oxidizing) test gas concentration. The results are plotted in the inset of Fig. 7(a) in a double-logarithmic plot. Even at the lowest gas concentrations, i.e., 5 ppm CO, the relative sensor resistance was well above the noise level with values of about 1.5. At 500 ppm CO, a decrease in resistance to about 1/4th of its value in dry air was detected. The resulting slope value, which serves as a measure of sensitivity, was −0.22. The response time t_{90} upon exposure to 5 ppm CO was 260 s, and recovery time was about 15 min.

When reducing the operating temperature, the response towards CO was found to decrease dramatically, and at 125°C, no significant response was observed over the entire concentration range. The results are summarized in Table 1, which combines measurements performed on three different specimens to ensure reproducibility of the reported results.

When the sensor was exposed to NO_2 over a concentration range from 0.5 ppm to 50 ppm at the temperature of 225°C, a steep resistance increase was observed as shown in Fig. 7(b), which is in agreement with the expected behavior of *n*-type metal oxides in the presence of oxidizing gases [28, 29].

Even at operating temperatures below 200°C, a rapid, significant change in resistance is observed. Over the entire temperature range, NO_2 response is found to be more pronounced than the response towards CO. Again, the relative change in sensor resistance R/R_0 yielded values well above noise levels even when exposed to trace NO_2 concentrations as low as 500 ppb (0.5 ppm). The response time and recovery time of SnO_2 fiber mats against NO_2 gas (at 5 ppm) were 400 s and 200 s, respectively.

According to the standard model of interaction between a reducing gas and a semiconducting oxide discussed for example in detail in Ref. [30] or [31], oxygen chemisorbs on SnO_2 surfaces in air, trapping charge carriers (electrons) and leading to a depletion layer. Incoming CO reacts with the adsorbed oxygen species. In this redox process, electrons previously trapped by the oxygen adions are de-trapped and become available for conduction. The

Table 1 Response towards CO at different temperatures.

T/°C	Slope value	Ro/R at 5ppm CO	Ro/R at 500ppm CO
125	−0.004	1	1.01
150	−0.02	1.05	1.13
155	−0.02	1.01	1.11
185	−0.03	1.03	1.18
225	−0.06	1.05	1.39
250	−0.07	1.35	1.9
300	−0.22	1.4	3.8
345	−0.19	1.1	2.4
390	−0.18	1.1	2.3

corresponding depletion layer width decreases, and a decrease of resistance in the presence of reducing gases is observed. In general, one would expect a high sensitivity even at low temperatures for devices with a high catalytic activity for CO oxidation. For example, a high specific surface area, determined by BET was found to be 73.5 m²/g for calcined SnO_2 nanofiber mats prepared with the inclusion of the thermo-compression step. However, the temperature dependent CO sensing mechanism is very complex, since it involves not only the reaction kinetics between CO and adsorbed oxygen, but also oxygen adsorption-desorption kinetics. The trend of decreasing sensitivity with decreasing temperatures below 300°C has been reported for a single SnO_2 nanowire [32] and for nano-crystalline porous thin films [33].

Independent measurements of the base resistance in dry air as a function of temperature were conducted from 125°C to 450°C, and the results are shown in Fig. 8. The resistance in air peaks at around 300°C, the same point at which the highest sensitivity values were observed. This suggests that the sensitivity maximum is related to the temperature at which maximum oxygen coverage is attained (i.e., the temperature of highest resistance in air). Similar results were reported for SnO_2 nanoribbons, [34] where a maximum CO sensitivity was observed at 300°C to 350°C. In this context, it should also be mentioned that at temperatures below 200°C, other adsorbed oxygen species like O_2^- are probably present at the sensor surface [35]. This might also influence the catalytic activity and its effect on conductance.

From the data presented in Fig. 7(b), it is possible to estimate the detection limit for NO_2 of the SnO_2 nanofiber sensors. Using the slope values determined from the double-logarithmic response plot (see inset of Fig. 7(b), and Table 2), the sensor resistance R was extrapolated to lower P_{NO2} values. The lower detection limit (LDL) was determined using the conventional definition LDL = gas concentration at which the sensor signal is equivalent to $3{\cdot}\sigma$, where σ denotes the standard deviation of the baseline measurements [36]. A detection limit of 150 ppb at 185°C was found. This detection limit is lower than that reported for other nanoscaled SnO_2 devices, e.g. SnO_2 nanofibers, which have been demonstrated to detect 3 ppm NO_2 at room temperature under UV illumination [37].

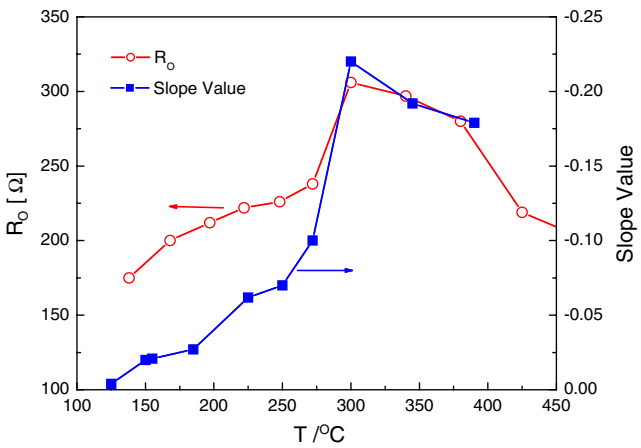

Fig. 8 Base resistance in dry air (*left axis*) and sensitivity towards CO (*right axis*) as a function of operating temperature. Resistance in air peaks around 300°C, and at the same point, the highest sensitivity values were observed

Table 2 Response towards NO_2 at different temperatures.

T/°C	Slope value	R/R_0 at 0.75 ppm NO_2	R/R_0 at 50 ppm NO_2
125	2.2	1.39	422
155	1.51	3.54	256
185	1.45	3.67	368
225	1.09	1.06	86

In contrast to the CO response, the sensitivity to NO_2 increased with decreasing temperature. This observation can be explained as follows. In the literature, the sensitivity of tin oxide towards NO_2 is generally attributed to an adsorption effect. Details of this process have been reported in detail in Ref. [38–40] (and references therein). Tin oxide surfaces tend to strongly adsorb NO_2, mostly as nitrato (NO_3^-) species [37, 39], which replace the oxygen at the surface. According to the results presented in Ref. [38], some of the NO_2-related nitrato adsorbates are very stable with high binding energies. By first principles calculations, a high net charge transfer from the semiconductor to these adsorbates was determined, thus explaining the pronounced conductivity drop in the presence of NO_2.

4 Conclusions

In summary, SnO_2 nanofiber mats, prepared by a combined electrospinning-thermo-compression procedure, exhibit attractive NO_2 and CO sensing characteristics. In particular, as determined by extrapolation of actual sensor tests, sub-ppm levels of NO_2 can be detected at temperatures below 200°C, attributed to the unique surface structure of the nanofiber mats. This points to the potential of accessing reduced operating temperatures with the present synthesis method, a significant advantage when compared to conventional microscaled gas sensor devices requiring higher temperature operation. In particular, this unique process-modification, i.e., thermo-compression step for electrospinning, opens up new opportunities for processing novel materials with enhanced surface activity, important for technological applications such as gas and chemical sensors as demonstrated in this work. Moreover, the ability to control the

geometrical structure of such electrospun nanofiber mats will enable systematic investigation of property-microstructure correlations in different classes of semiconducing metal-oxides for various applications.

Acknowledgement The authors gratefully appreciate Dr. Kathy Sahner's support for sensing characterization and helpful discussion. This work was supported by KIST research program of one of the authors (I.-D. K) under Grant No. 2E21760. The work at MIT was supported, in part, by the National Science Foundation under Grant No. ECS-0428696.

References

1. V.V. Sysoev, J. Goschnick, T. Schneider, E. Strelcov, A. Kolmakov, Nano Lett. **7**, 3182 (2007)
2. M.C. McAlpine, H. Ahmad, D. Wang, J.R. Heath, Nat. Mater. **6**, 379 (2007)
3. Y. Wang, X. Jiang, Y. Xia, J. Am. Chem. Soc. **125**, 16176 (2003)
4. Z. Zhong, D. Wang, Y. Cui, M.W. Bockrath, C.M. Lieber, Science **302**, 1377 (2003)
5. J.E. Allen, E.R. Hemesath, D.E. Perea, J.L. Lensch-Falk, Z.Y. Li, F. Yin, M.H. Gass, P. Wang, A.L. Bleloch, R.E. Palmer, L.J. Lauhon, Nat. Nanotech. **3**, 168 (2008)
6. L. Shi, Y. Xu, S. Hark, Y. Liu, S. Wang, L.M. Peng, K. Wong, Q. Li, Nano Lett. **7**, 3559 (2007)
7. M. Law, L.E. Greene, J.C. Johnson, R. Saykally, P. Yang, Nat. Mater. **4**, 455 (2005)
8. J. Duan, J. Gong, H. Huang, X. Zhao, G. Cheng, Z.Z. Yu, S. Yang, Nanotechnology **18**, 055607 (2007)
9. Z.L. Wang, Annu. Rev. Phys. Chem. **55**, 159 (2004)
10. W. Zhu, W. Wang, H. Xu, J. Shi, Mater. Chem. Phys. **99**, 127 (2006)
11. Y. Wang, H.C. Zeng, J.Y. Lee, Adv. Mater. **18**, 645 (2006)
12. I.D. Kim, A. Rothschild, B.H. Lee, D.Y. Kim, S.M. Jo, H.L. Tuller, Nano Lett. **6**, 2009 (2006)
13. Y. Wang, I. Ramos, J.J. Santiago-Aviles, IEEE Sens. J. **7**, 1347 (2007)
14. G. Wang, Y. Ji, X. Huang, X. Yang, P.I. Gouma, M.J. Dudley, Phys. Chem. B **110**, 23777 (2006)
15. O. Landau, A. Rothschild, E. Zussman, Chem. Mater. **21**, 9 (2009)
16. S.H. Choi, G. Ankonina, D.Y. Youn, S.G. Oh, J.M. Hong, A. Rothschild, I.D. Kim, ACS Nano **3**, 2623 (2009)
17. Z. Liu, D.D. Sun, P. Guo, J.O. Leckie, Nano Lett. **7**, 1081 (2007)
18. S. Li, C. Shao, Y. Liu, S. Tang, R. Mu, J. Phys. Chem. Solids **67**, 1869 (2006)
19. I.D. Kim, J.M. Hong, B.H. Lee, D.Y. Kim, E.K. Jeon, D.K. Choi, D.J. Yang, Appl. Phys. Lett. **91**, 163109 (2007)
20. E. Formo, E. Lee, D. Campbell, Y. Xia, Nano Lett. **8**, 668 (2008)
21. P.I. Gouma, Rev. Adv. Mater. Sci. **5**, 147 (2003)
22. K.M. Sawicka, A.K. Prasad, P.I. Gouma, Sens. Lett. **3**, 31 (2005)
23. A. Rothschild, H.L. Tuller, J. Electroceram. **17**, 1005 (2006)
24. I.D. Kim, A. Rothschild, H. Takeo, H.L. Tuller, Nano Lett. **6**, 193 (2006)
25. J.W. Gardner, Semicond. Sci. Technol. **4**, 345 (1989)
26. A. Rothschild, Y. Komem, J. Electroceram. **13**, 670 (2004)
27. A. Rothschild, Y. Komem, J. Appl. Phys. **95**, 6374 (2004)
28. D.E. Williams, Sens. Actuators B **57**, 1 (1999)
29. V. Kobrinsky, A. Rothschild, V. Lumelsky, Y. Komem, Y. Lifshitz, Appl. Phys. Lett. **93**, 113502 (2008)
30. N. Barsan, U. Weimar, J. Phys. Condens. Matter **15**, R813 (2003)
31. A.M. Azad, S.A. Akbar, S.G. Mhaisalkar, L.D. Birkefeld, K.S. Goto, J. Electrochem. Soc. **139**, 3690 (1992)
32. A. Kolmakov, Y. Zhang, G. Cheng, M. Moskovits, Adv. Mater. **15**, 997 (2003)
33. Z. Jin, H. Zhou, Z.L. Jin, R.F. Savinell, C.C. Liu, Sens. Actuators B **52**, 188 (1998)
34. S. Kandasamy, A. Trinchi, W. Wlodarski, E. Comini, G. Sberveglieri, Sens. Actuators B **111–112**, 111 (2005)
35. A. Gurlo, Chem. Phys. Chem. **7**, 2041 (2006)
36. N. Barsan, J.R. Stetter, M. Findlay Jr., W. Göpel, Anal. Chem. **71**, 2512 (1991)
37. M. Law, H. Kind, B. Messer, F. Kim, P. Yang, Angew. Chem. Int. Ed. **41**, 2405 (2002)
38. A. Maiti, J.A. Rodriguez, M. Law, P. Kung, J.R. McKinney, P. Yang, Nano Lett. **3**, 1025 (2003)
39. E. Leblanc, L. Perier-Camby, G. Thomas, R. Gibert, M.M. Primet, P. Gelin, Sens. Actuators B **62**, 67 (2000)
40. C. Baratto, E. Comini, G. Faglia, G. Sberveglieri, M. Zha, A. Zappettini, Sens. Actuators B **109**, 2 (2005)